Journal of Magnetism and Magnetic Materials 555 (2022) 169358

Contents lists available at ScienceDirect

Journal of Magnetism and Magnetic Materials

journal homepage: www.elsevier.com/locate/jmmm

F^+ center exchange mechanism and magnetocrystalline anisotropy in Ni-doped 3C-SiC

Gyanti Prakash Moharana [a], Rahul Kothari [b], S.K. Singh [c], P.D. Babu [d], Harish Kumar Narayanan [a,*]

[a] Advanced Magnetic Materials Laboratory, Department of Physics, IIT Madras, Chennai 600036, India
[b] Department of Physics and Astronomy, The University of the Western Cape, Cape Town 7535, South Africa
[c] Advance materials Lab, IMMT, Bhubaneswar 751013, India
[d] UGC-DAE Consortium for Scientific Research Mumbai Centre, R-5 shed, BARC, Trombay, Mumbai 400085, India

A B S T R A C T

Towards the development of a magnetic semiconductor suitable for spintronic device applications in extreme environments, we explored the possibility of inducing magnetic interaction in SiC by doping Nickel. The X-ray diffraction and Raman Spectroscopy studies confirm the incorporation of Ni into the host lattice. The magnetic measurements and electron spin resonance studies indicate the presence of room temperature ferromagnetic interaction in the system. The Curie temperature of 1, 3, and 5% Ni-doped samples have been found to be 420 K, 520 K, and 540 K respectively. Electron spin resonance study reveals that the valence state of Ni is 2^+, which implies the creation of vacancies at both Silicon (V_{Si}) and Carbon (V_C) sites as they are tetravalent. The change in magnetization of the system with an increase in dopant concentration is consistent with the variation in the number of vacancies and free holes. The analysis of magnetization data using the Law of approach to saturation shows that the anisotropic constant decreases with an increase in temperature. The long-range magnetic interaction in the system is explained using the F^+ center exchange mechanism.

1. Introduction

The ever increasing demand for expansion of memory storage capacity and raising the speed of information processing and the constraints imposed by thermal effects and quantum effects on miniaturization of devices below a certain limit leads to the novel idea of exploiting the spin of the electrons in addition to its charge for device applications. Since information is stored magnetically and processed electronically the integration of magnetics with electronics not only results in an integration of these functions in a single device but can also lead to the development of novel multifunctional devices. As electronic devices are based on semiconductors and the technology for the fabrication of semiconductor devices has been well developed, one of the research focus in the emerging technology area of spintronics is inducing magnetic interactions in semiconductors [1,2,3]. After some unsuccessful attempts at doping transition metal ferromagnetic elements in the well know semiconductor Si, the focus shifted to other semiconductors. The theoretical prediction on room temperature ferromagnetism in 5% Mn-doped wide band gap semiconductors GaN and ZnO by Dietl *et al.* [4] lead to a flurry of research activity on dilute magnetic semiconductors (DMS) [5–13]. But the controversies regarding the nature of magnetic interaction in DMS remain. However, the report on the observation of intrinsic ferromagnetism in Co-doped TiO_2 films through depth-resolved low energy muon spin rotation experiments by Saadaoui *et al.* [14] has strengthened the belief that it is indeed possible to induce long-range magnetic interactions in wide band gap semiconductors through transition metal doping. Long Lin *et al.* showed through theoretical studies that co-doping Mn and Co atoms in the wideband gap semiconductor SnO_2 stabilizes the ferromagnetic state [15,16]. Theoretical studies also show that dilute magnetic systems could be used for gas sensing applications [17–19].

A certain class of carbon-based materials and wide band gap semiconductors could display ferromagnetism when specific defects are introduced in it. This phenomenon in which magnetic interaction could be realized in the materials which contain neither unpaired 3d nor 4f electrons is known as defect-induced magnetism (d^0). It is a localized effect that depends upon the distribution of defects as well as the distance between divacancies. As pure SiC exhibits defect-induced weak magnetism which cannot scale into the entire volume, there have been studies on p-type carrier doping to enhance the strength of d^0 magnetism. In addition to introducing p-type carriers if the dopant also carries a magnetic moment then it may be an added advantage [20–24].

The high electron drift velocity, breakdown voltage, thermal conductivity, and radiation resistance of the wide-bandgap semiconductor

* Corresponding author.

https://doi.org/10.1016/j.jmmm.2022.169358
Received 10 January 2022; Received in revised form 27 March 2022; Accepted 11 April 2022
Available online 15 April 2022

SiC make the material attractive for the fabrication of devices required to work in a harsh environment [25–28]. Hence inducing magnetic interaction in this material will enable the fabrication of spintronic devices suitable for device applications under extreme conditions.

SiC has many allotropes. While most of them have a hexagonal structure with a different number of stacks of SiC layers, the β-phase (3C-SiC) has a cubic structure and forms at a relatively lower temperature. There have been reports in the literature on the magnetic properties of 3d transition metal doped 6H-SiC and 3C-SiC [29–37]. Among the 3d transition metal dopants, Nickel has received less attention as the earlier reports on Ni ion implantation in SiC and Ni doping in thin-film SiC showed magnetic ordering below room temperature [29,36]. In this report, we have carried out a detailed investigation on the nature of magnetic interactions and magnetocrystalline anisotropy in Ni-doped 3C-SiC synthesized by spark plasma synthesis using magnetic measurements and spectroscopic investigations.

2. Experimental details

The Ni-doped 3C-SiC polycrystalline samples were prepared by carbothermal reduction method using Rice husk and $Ni(Cl_2)6H_2O$ as the starting material. The details of the synthesis of SiC from rice husk can be found elsewhere [38,39]. The synthesis was carried out using a steady Argon gas flow of 2-LPM, current-50A, and load voltage-300 V. The synthesis of the material was carried out at 1600 °C and the time duration was 15mins. The possible reactions for the formation of SiC from Rice husk can be written as,

$$SiO_2\ (amorphous) + 3C\ (amorphous) \rightarrow SiC + 2CO$$

The chemical reaction for Ni incorporation into SiC is as follows

$$NiCl_2(6H_2O) + SiO_2 + 4C \rightarrow SiNiC + 2HCl\uparrow + 5H_2O\uparrow + 3CO\uparrow \quad (1)$$

The structural characterization was carried out employing a Rigaku Smart lab X-ray diffractometer with copper K_α radiation and Horiba Jobin-Yvon HR-800 Micro Raman spectrometer with 488 nm laser wavelength. The microstructural investigation was done using a Transmission electron microscope (TEM) Technai model with 200 kV operating voltage. A Quantum Design 9 Tesla PPMS based - Vibrating Sample Magnetometer (VSM) and a SQUID VSM were employed for the low-temperature magnetization measurements. The valence state of unpaired electrons, dipolar interaction, and anisotropy in the system was probed using the JEOL model JES FA 200electron spin resonance (ESR) spectrometer.

3. Results and discussion

A. Structure and Microstructure

The XRD patterns (Fig. 1 (a)) recorded on the samples reveal that all the samples have crystallized in the cubic 3C-SiC phase. The XRD peaks exhibit a shift towards high angles as the Ni concentration increases which indicate the incorporation of Ni into the host lattice.

Even though the ionic radius of Ni^{2+} is larger than Si^{4+} which is expected to result in lattice expansion which should cause the XRD peaks to shift to a lower angle, the creation of V_{Si} vacancies to maintain charge neutrality may tend to decrease the interplanar spacing. If the latter effect dominates over the former then there will be a net decrease in interplanar spacing which will result in XRD peak shift to higher angles [40,41].

The peak shift towards higher wave number [Transverse Optical (TO) and Longitudinal Optical (LO)] and the increase in peak width of the Raman spectral lines with the increase in Ni doping as shown in Fig. 1(b) indicates the formation of defects and some local tetrahedral distortion as well as an increase in carrier concentration.

The High-resolution transmission electron microscope (HRTEM) images (Fig. 2.a -d) show the presence of stacking faults. The crystalline quality of the samples investigated using selected area electron diffraction (Fig. 2.e-h) shows a diffraction pattern which could be indexed to Cubic symmetry with space group,$F\bar{4}3m$. The crystalline quality of the sample has been reduced a little bit because of the defect formation during the synthesis.

B. Magnetization Studies:

Isothermal magnetization and FC-ZFC curves have been recorded in the temperature range 5 K- 350 K using SQUID vibrating sample magnetometer (VSM) and PPMS based VSM. Fig. 3(a, b, c) represents the magnetic hysteresis (M−H) plots recorded on as-prepared Ni (1, 3, 5) % doped samples, at 5 K, 80 K, and 300 K.The expanded low field part of the M−H response clearly depicts the hysteretic characteristics (Inset Fig.(i)). The inset Fig. (ii) shows the FC-ZFC plots recorded at 1kOe applied field in the temperature range 5 K to 350 K. In all these curves the bifurcation between FC and ZFC curves sustains up to room temperature, which indicates that ferromagnetic interaction is present in the system. Upon annealing the sample at 1200 °C for 10hrs, magnetic measurement was carried out on the samples from 5 K to 350 K.

The DC magnetization measurements (Fig. 3.a-c) on all the as-prepared Ni-doped 3C-SiC samples show a nonlinear magnetic response with clear hysteresis loop opening (Inset Fig. i) at the three temperatures 5 K, 80 K, and 300 K at which the measurements were

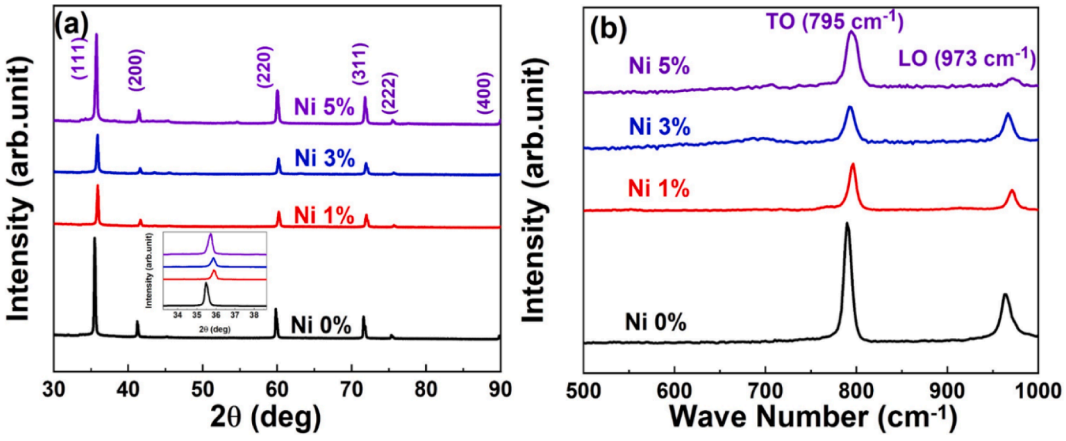

Fig. 1. (a) XRD pattern of undoped and Ni-doped 3C-SiC. Inset shows zoomed portion of (1 1 1) peak (b) Raman spectra of undoped and Ni-doped 3C-SiC. A clear shift in peak position with respect to the undoped sample has been observed in all the doped samples.

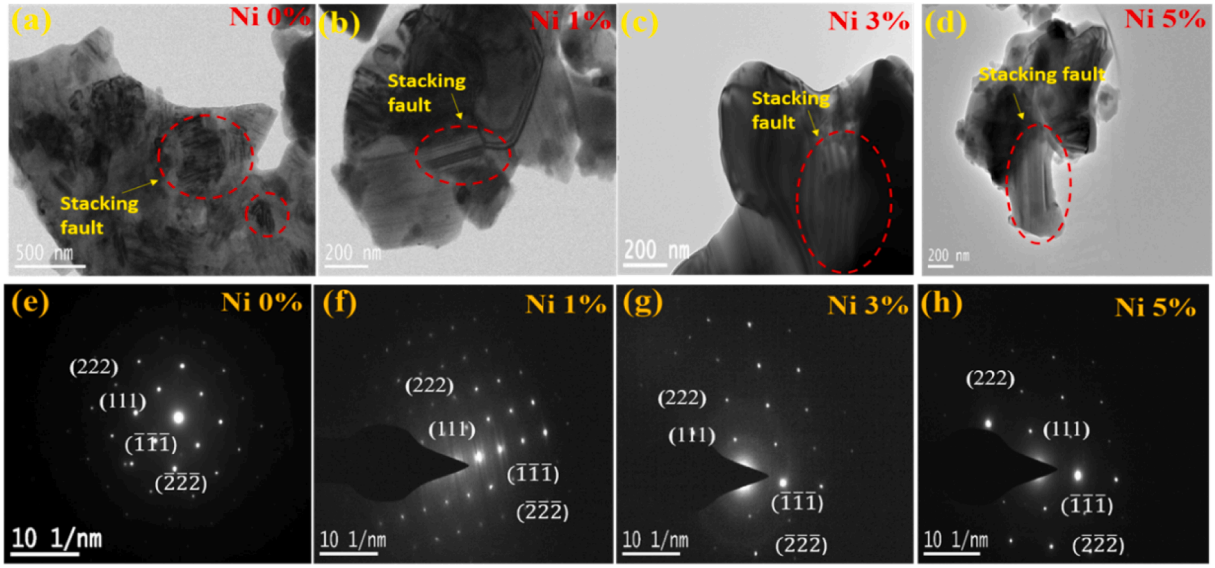

Fig. 2. (a, b, c, d) HRTEM image showing the presence of stacking faults and SAED pattern (e, f, g, h) showing the diffraction spots indexed to cubic phase with space group $F\bar{4}3m$.

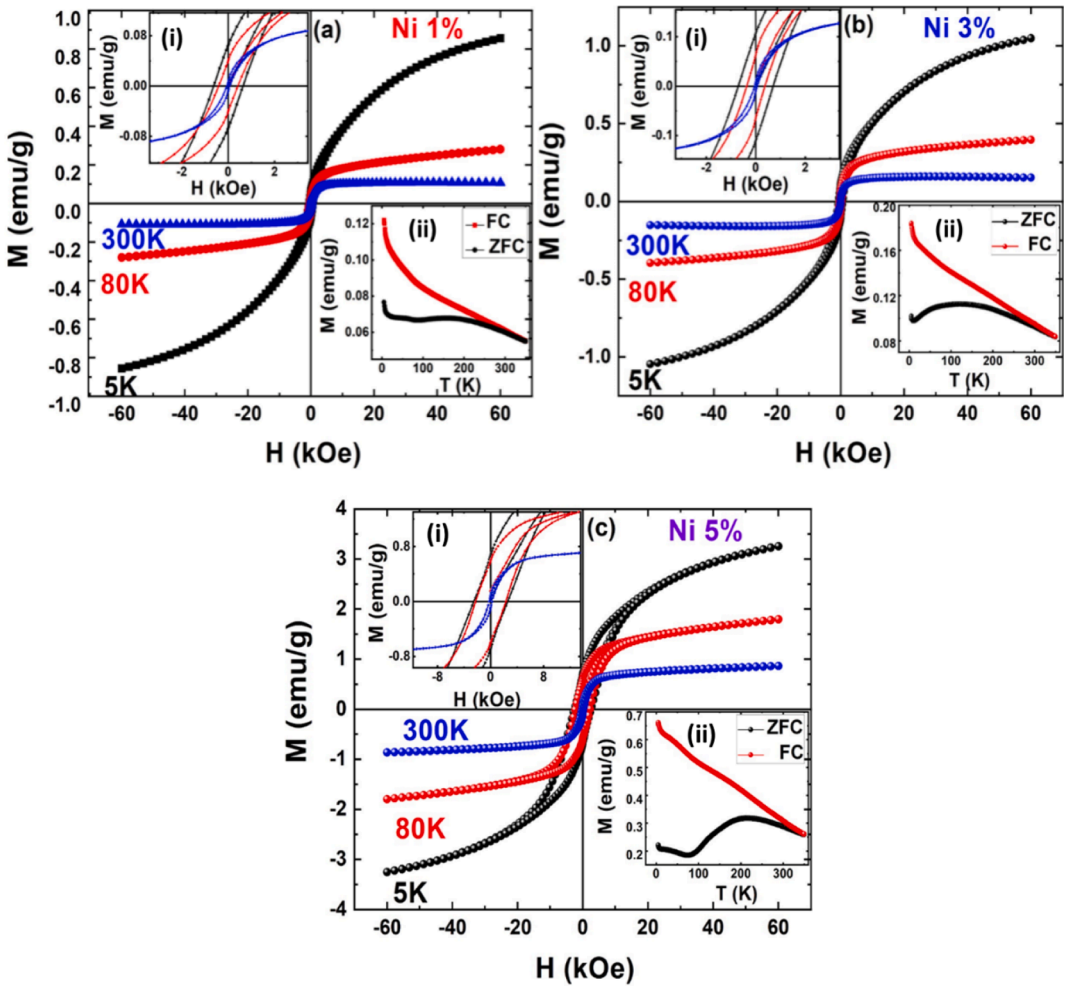

Fig. 3. (a, b, c) M−H plot of as prepared Ni-doped 3C-SiC samples recorded at three different temperatures. Inset (i) Expanded view of the low field M−H response showing hysteresis (ii) FC-ZFC plot recorded at 1kOe applied field in each sample.

carried out which is indicative of ferromagnetic interactions present in the system. Among the three doped samples, the 5% Ni-doped sample exhibits maximum magnetization and the largest hysteresis loop area which shows that the ferromagnetic interactions are the strongest in this material. The zero filed Cooled (ZFC) and field Cooled (FC) magnetization measurements carried out at 1 kOe magnetic field show clear bifurcation of the ZFC and FC response (Inset Fig. ii) which sustains up to room temperature (RT) indicating the presence of ferromagnetic interactions up to RT.

The magnetic measurements were repeated after annealing the samples at 1200 °C for 10 hrs. Fig. 4 (a-c) shows the hysteresis loops recorded on the annealed samples at three different temperatures 5 K, 80 K, and 300 K. The inset figures (i) and (ii) show the expanded portion of the M−H loops in the low field regime and ZFC – FC curves recorded in the temperature range 0 to 350 K at 1 kOe respectively. No significant change in the overall magnetic response and the bifurcation in the FC-ZFC curves were observed but a reduction in hysteresis loop area was observed in all the annealed samples which could be due to the release of strain in the material after annealing.

However, it has been reported in the literature as well as observed by us that even pure 3C-SiC display ferromagnetic response at RT due to defects present in it [23]. But the magnetic moment value is at least 3 orders of magnitude smaller than that of the Ni-doped samples. The introduction of a transition metal element into the SiC matrix is expected to strengthen the magnetic interaction in the system.

Further, the substitution of Ni^{2+} in place of Si^{4+} can introduce (local) anisotropy in the system. From the analysis of magnetization data, the magnetocrystalline anisotropy and its role on the magnetic interactions in the system have been determined. The magnetization can be written as,

$$M(H,T) = \frac{2M_s}{\pi} tan^{-1}\left[\frac{H \pm H_C}{H_C} tan\left(\frac{\pi S}{2}\right)\right] + M_{SP} L\left(\frac{\mu H}{kT}\right) \quad (2)$$

Where, M_S, H_C, H, and S are the saturation magnetization, coercivity, applied field, and squareness of the M−H loop respectively [42,43]. The parameter S is given by the ratio of the remnant magnetization (M_r) to the saturation magnetization (M_S) [$S = M_r/M_S$]. The term M_{SP} is the superparamagnetic component of the magnetization and L is the Langevin function. The first term represents the ferromagnetic contribution and the second term gives the paramagnetic contribution. The Ni 5% doped 3C-SiC sample exhibits the maximum value of saturation magnetization and coercivity (Fig. 5.a, b).

Fig. 6 (a) shows the fit to the experimental M−H curve of annealed samples of Ni-doped 3C-SiC using Eq. (2). Using the fit to the semi-empirical Eq. (3) [44–46] the Curie temperatures (T_C) of the samples were determined by extrapolation of the M−T curves as shown in Fig. 6 (b).

$$M(T) = M(0)\left[1 - s(T/T_C)^{\frac{3}{2}} - (1-s)(T/T_C)^p\right]^\beta \quad (3)$$

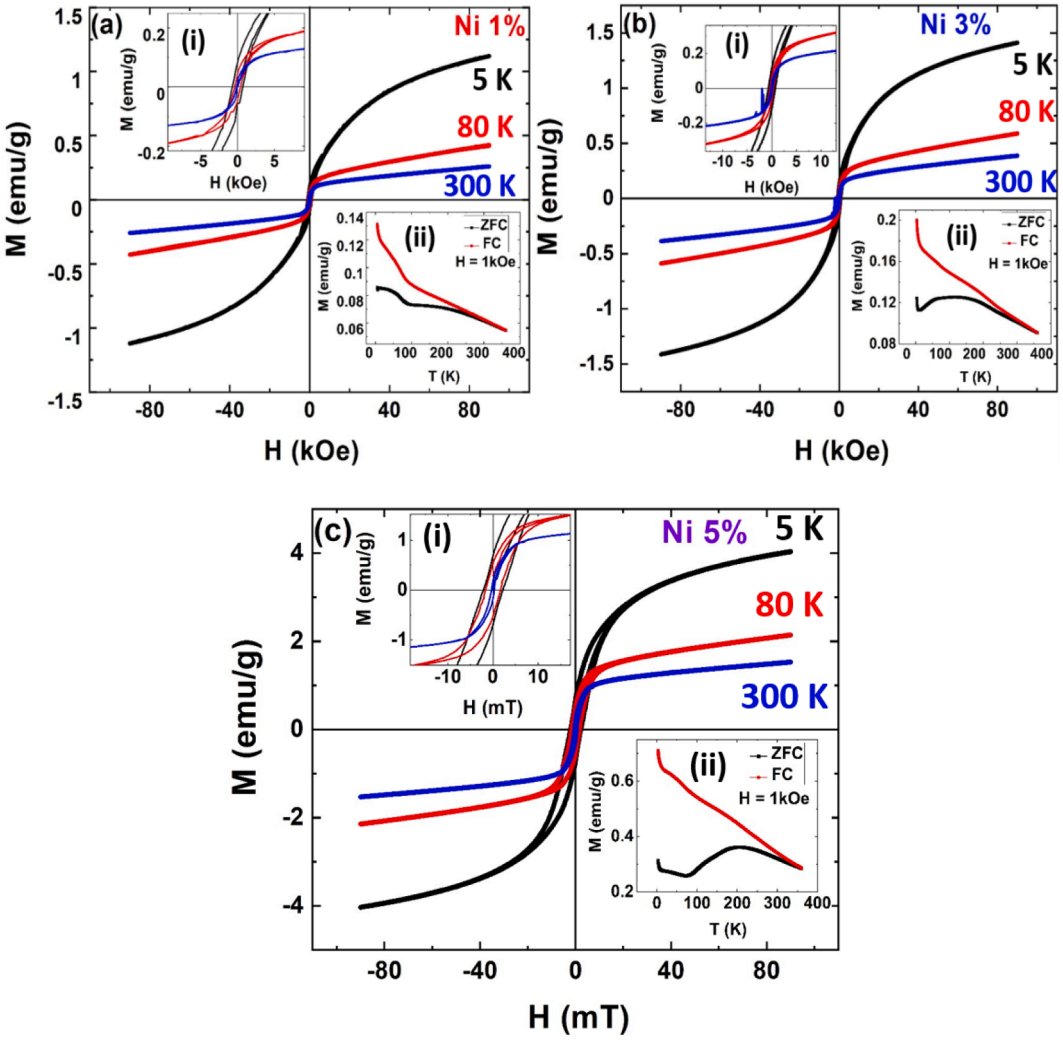

Fig. 4. (a, b, c) Magnetic Hysteresis recorded on annealed samples of Ni-doped 3C-SiC at three different temperatures. Inset (i) Expanded portion of the low field part of the hysteresis loops showing clear loop opening. (ii) Bifurcation of FC-ZFC plots recorded at 1kOe field.

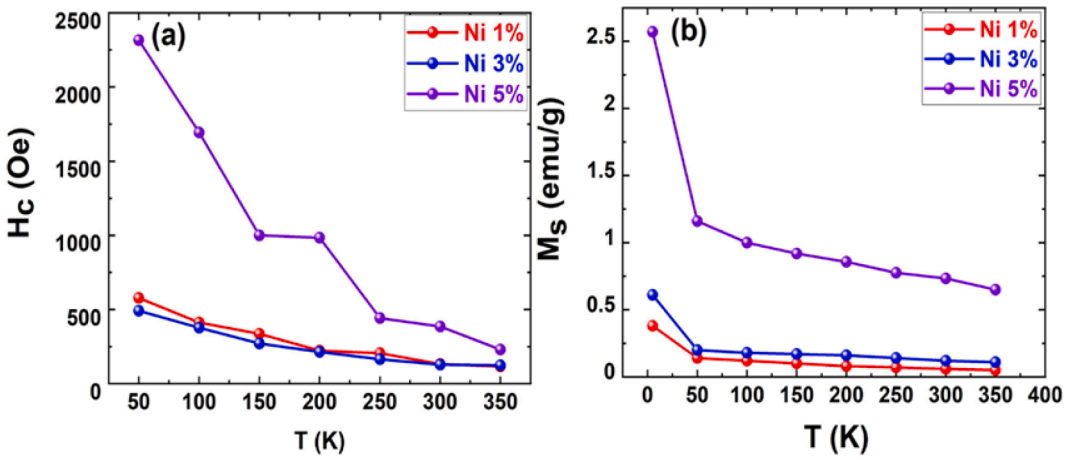

Fig. 5. (a) Variation of Coercivity and (b) Ms with Temperature for Ni-doped 3C-SiC. The solid lines are a guide to the eye.

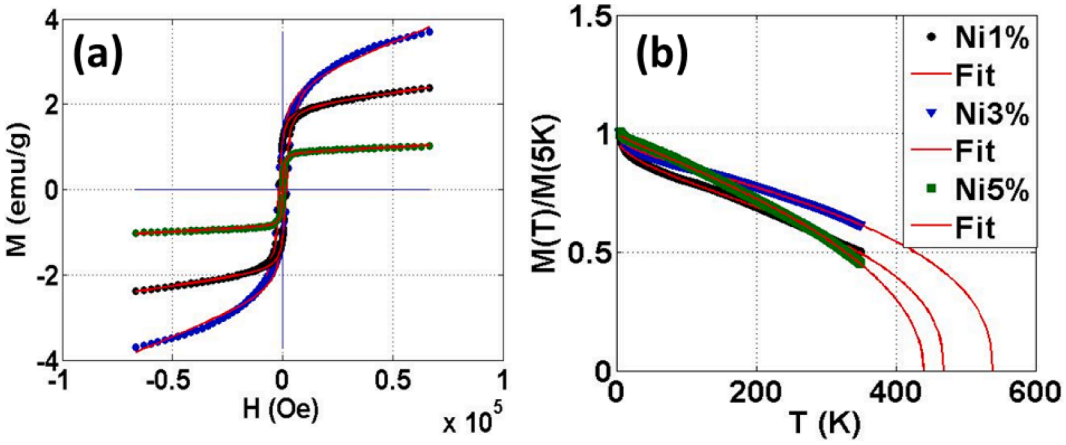

Fig. 6. (a) M–H plot of annealed Ni-doped samples with fit to Eq. (2) (b) Determination of Curie temperature by extrapolation of the fit to the M –T data using Eq. (3).

Where *M (0)* is magnetization at the initial temperature (5 K) and *s* is the shape factor. The value of *s* is found to be 0.40. A small value of $s \sim 0.40$ is a clear sign of long-range ferromagnetic order. The exponent *p* is a semi-empirical fit parameter which turns out to be 0.85. The value of the critical exponent of the order parameter, β is found to be 0.49 which is nearly equal to the theoretical mean value ($\sim 1/2$) that indicates long-range ferromagnetic order in the system. The Curie temperature of Ni-doped samples obtained by extrapolation of the fit to the M vs T data using modified Bloch's $T^{3/2}$ law (Eq. (3)) has been found to be 420 K, 520 K, and 540 K respectively for 1, 3, and 5% doping levels.

The Coercivity variation with temperature was analyzed using the Bound Magnetic Polaron model (BMP) Eq. (4).

$$H_C = H_{CO}\left[1 - \left(\frac{T}{T_B}\right)^{1/2}\right] \tag{4}$$

Where, T_B is the blocking temperature, *T* is the temperature, and H_{CO} is the coercivity at T = 0 K. As the fits to the experimental data on temperature variation of coercivity, assuming temperature-independent fixed BMP size shows considerable deviation (Fig. 7), a modified BMP model proposed by Coey *et al.* [47] which assumes magnetic cluster size variation with temperature and defect mediated exchange mechanism was considered to set up a long-range range magnetic order in the system, there has to be a sufficient number of BMPs with the required size to reach the percolation threshold limit. Assuming a particle composed of N spherical polarons of radius r, volume can be expressed as $V = \frac{4}{3}N\pi r^3$. There is a relation between polaron radius and dielectric constant ε of

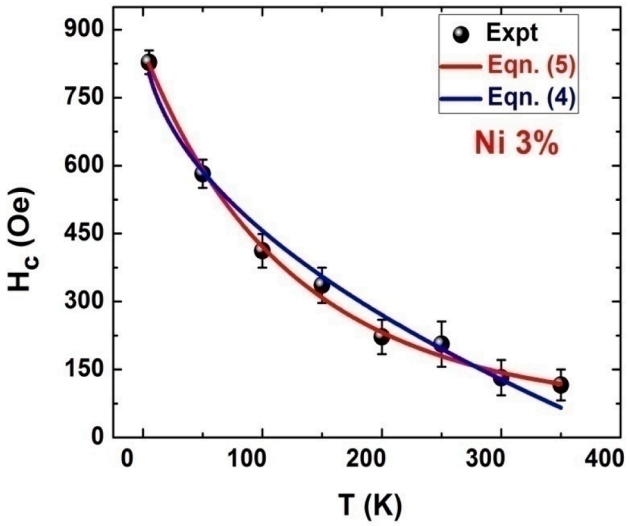

Fig. 7. Coercive field variation with temperature for 3% Ni-doped 3C-SiC. The solid lines are fit to the unmodified (Eq. (4)) and modified (Eq. (5)) coercivity equation for BMPs.

the materials as $r = \varepsilon(m/m^*)a_0$, [47] were, m is the electron mass, m* is the effective mass of the donor electrons, and a_0 is the Bohr radius (0.53 Å). Assuming the effective mass to be a constant, the polaron radius can be approximated in terms of dielectric constant as $r = a_0\varepsilon$. The polaron exchange mechanism can result in magnetically active regions in TM doped 3C-SiC when the size of the magnetic clusters changes with temperature and can be explained assuming first-order temperature dependence of the dielectric constant$\varepsilon(T) = \varepsilon_{TO} + \alpha T$. Where ε_{TO} is the Static Dielectric constant and α is the linear expansion coefficient. To determine the magnetic coercivity variation with temperature, the blocking temperature could be expressed in terms of anisotropy constant and volume as $T_B = KV/25k_b$, in Eq. (4) [48].

Using this expression, Eq. (4) can be modified as given in Eq. (5) [49].

$$H_C = H_{CO}\left[1 - \left(\frac{25k_BT}{NK(4/3)\pi a_0^3(\varepsilon_{TO} + \alpha T)^3}\right)^{1/2}\right] \quad (5)$$

This equation fits quite well with the experimental data as shown in Fig. 7. Hence the long-range magnetic order in Ni-doped 3C-SiC can be explained using the temperature-dependent percolation threshold for BMPs.

C. Magneto crystalline Anisotropy

The magnetocrystalline anisotropy and its role on the magnetic interactions in the system have been analyzed by using the "Law of Approach to Saturation" to the high field isothermal magnetization data as it helps to obtain an approximate estimation of anisotropy constant in a polycrystalline magnetic material [50 –53]. From the best fit to the experimental data (Fig. 8(a) the effective anisotropy constant, K_E was determined using the values of the parameters obtained. The value of K_E calculated at 5 K & 350 K for 5 % Ni-doped 3C-SiC sample are 2.15×10^5 erg/cm^3 and 0.85×10^5 erg/cm^3 respectively. The K_E values show a slight increase initially and reach a peak value around 50 K and then decrease monotonically as the temperature increases as shown in Fig. 8 (b). The temperature dependence of the anisotropic constant accounts for the high coercivity values observed in the low-temperature regime and the weakening of the magnetic interactions as the temperature rises.

4. Mechanism of magnetization

The magnetic properties of Dilute Magnetic Semiconductors (DMS) could depend upon many parameters such as concentration and distribution of TM ions, types and concentration of defects, and nature of doping (n-type or p-type). The long-range magnetic order in DMS has been explained based on either the Zener model (Mn-doped GaN) or hole-mediated exchange interaction proposed by Diet *et* al (Mn-doped ZnO). But experimental results have shown clearly the presence of defects in the DMS system and hence there have been theoretical models proposed based on defect-mediated magnetic interactions. Among the various theoretical models developed to explain FM in DMSs, the percolation model developed by Kaminski and Das Sarma is an important mechanism [54]. In the case of the oxide DMS system, the Bound Magnetic Polaron (BMP) model of Coey et al. has been used to explain long-range magnetic order. As the defects (Vsi, Vc) present in the system may play important role in establishing long-range ferromagnetic order in transition metal-doped SiC we checked the applicability of the BMP model [47] to understand the magnetic response of the system. In the high-temperature range, the saturation magnetization M_S can be taken approximately equal to M_{eff} to estimate the number of BMPs. The experimental isothermal magnetization plots recorded at different temperatures along with the BMP model fit to the data are shown in Fig. 9 (a-c) for all the Ni-doped samples. The M−H plots after subtraction of the paramagnetic contribution exhibiting clear saturation are shown in Fig. 10 (a-c). The parameters obtained from the BMP fit to the M−H data are given in Table.4.1. The number density of BMP estimated from the parameters obtained from the model fit is found to be the order of 10^{18} per cm^3 as shown in the Table. But the BMP number density required to achieve percolation to set up long-range ferromagnetic order is 10^{20} per cm^3 in oxide DMS system (ZnO) [55]. As the number density of BMP in Ni-doped 3C-SiC is two orders of magnitude smaller than the value needed for percolation, defect alone cannot be held responsible for room temperature ferromagnetism in the system. Hence the high-temperature ferromagnetic response of the system cannot be explained by the BMP percolation model. However, the high-temperature synthesis of Ni-doped 3C-SiC sample provides a favorable condition to form defects such as (V_{Si},V_C, V_{SiC}). The presence of such defects has already been confirmed by FC - ZFC measurements on pure 3C-SiC. Similar to the role of Mn ion in Mn-doped ZnO DMS, in the SiC system, Ni acts as a charge donor. The presence of silicon and carbon vacancies in 3C-SiC is favorable for the occupation of holes due to the activation of acceptor states. The replacement of Si^{4+} ions by Ni^{2+} will produce two holes. As the Ni concentration increases, the number of holes also increases. The analysis of Raman spectra has confirmed that the carrier concentration increases with an increase in nickel concentration. This suggests that a model based on carrier-mediated (hole) interaction can be used to explain the long-range ferromagnetic order in the Ni-doped 3C-SiC. In addition to this, grain boundary and dislocation-like defects can play a vital role in inducing the long-range ferromagnetic order in the system

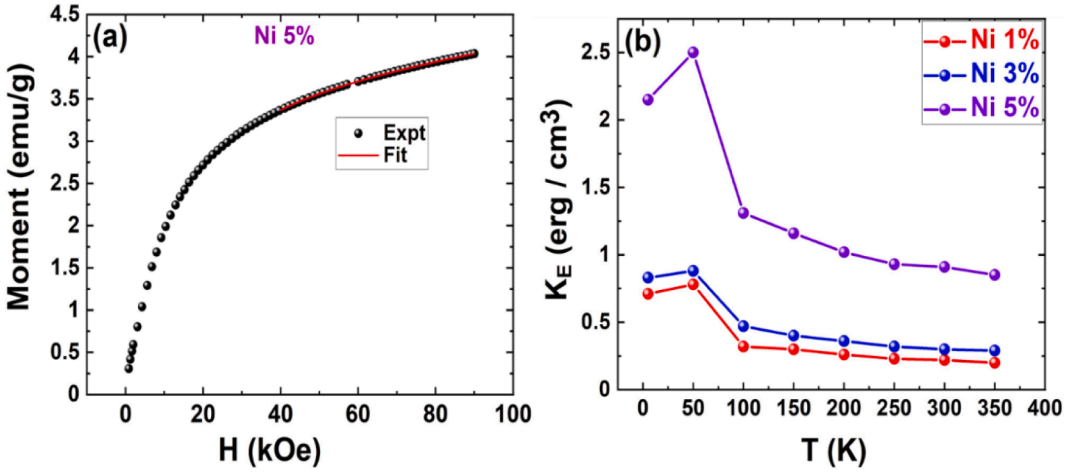

Fig. 8. (a) Law of approach to saturation model fit to the high field isothermal magnetization data. (b) Variation of effective anisotropy constant, K_E with Temperature for Ni-doped 3C-SiC. The solid lines are a guide to the eye.

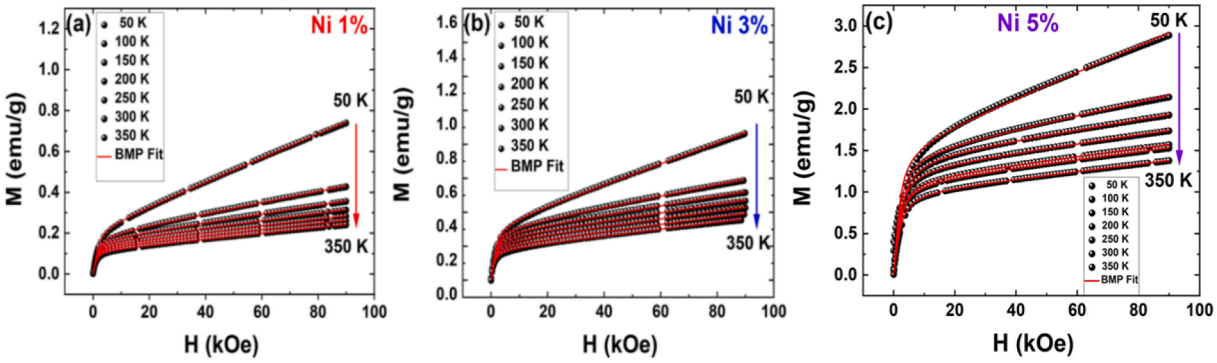

Fig. 9. The Bound Magnetic Polaron (BMP) model fits to the isothermal magnetization data of Ni-doped 3C-SiC.

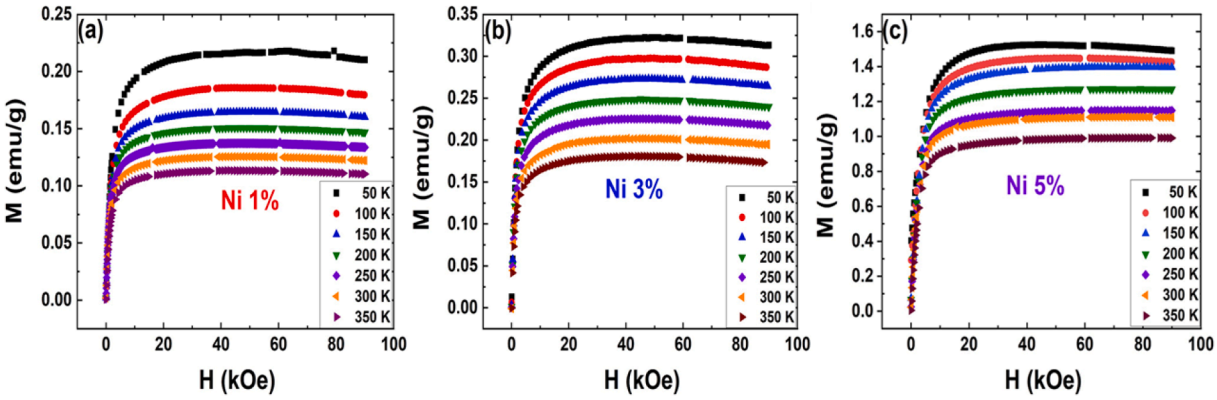

Fig. 10. M−H Plots of Ni-doped 3C-SiC after subtraction of paramagnetic Contribution.

Table 4.1
The parameter obtained from the BMP model fit to the isothermal magnetization data of Ni-doped 3C-SiC samples.

Ni	**1%**			
T(K)	M_0 (emu/g)	$M_{eff} \times 10^{-17}$ (emu)	$\chi_m \times 10^{-6}$ (emu/gOe)	$N \times 10^{16}$ (cm^{-3})
50	0.21	0.75	5.80	8.8
100	0.18	1.58	2.74	3.6
150	0.16	2.79	2.16	1.8
200	0.15	4.08	1.84	1.1
250	0.13	5.41	1.65	0.77
300	0.12	6.66	1.53	0.57
350	0.11	7.87	1.43	0.44
T(K)	**3%**			
50	0.32	0.80	6.10	12.8
100	0.29	1.78	3.35	5.22
150	0.27	2.87	2.79	3.01
200	0.24	4.05	2.50	1.90
250	0.22	5.07	2.30	1.39
300	0.20	6.41	2.15	1.00
350	0.17	7.87	2.03	0.69
T (K)	**5%**			
50	1.53	0.68	15.50	72.0
100	1.46	1.25	7.95	37.4
150	1.42	1.56	7.57	29.2
200	1.29	2.48	5.19	16.6
250	1.16	3.13	4.68	11.8
300	1.12	3.77	4.64	09.5
350	1.00	4.43	4.28	07.2

[33,56,57]. Considering the possibility of the existence of BMPs in the material and an increase in carrier concentration due to Ni doping, a modified BMP model has been used to explain the long-range magnetic order in Ni-doped 3C-SiC. The exchange interactions between a localized charge carrier trapped by defects (F^+ center) such as Vsi or Vc here, and many surrounding Ni^{2+} ions align all the Ni^{2+} spins around the carrier localization center resulting in the formation of a BMP. There are two possibilities for long-range magnetic interaction in the system. It can be achieved either by (i) direct overlapping of two polarons or (ii) indirect interaction between two polarons through a magnetic impurity. The nature of interaction will ultimately depend upon the number density of BMPs formed and the distance between them in the host matrix. The BMP number density in the Ni-doped 3C-SiC samples have been estimated to be 0.57×10^{16} cm^{-3}, 0.12×10^{17} cm^{-3}, and 0.95×10^{17} cm^{-3} in the 1, 3, and 5% Ni-doped samples respectively at RT which is not sufficient for direct overlap to reach the percolation limit. So the magnetic impurity may act as a kind of messenger to facilitate the exchange interaction among the BMPs to achieve ferromagnetism in the system. In addition to this, spontaneous spin polarization can be induced in the system due to strong hybridization between C 2p and Ni 3d orbitals [58 –60]. Hence the room temperature ferromagnetism exhibited by Ni-doped 3C-SiC can be explained as a combined effect of orbital hybridization and magnetic impurity-mediated BMPs. The lack of saturation observed in magnetization could be due to paramagnetic contributions from isolated charges trapped at vacancies (F – centers).

5. X-band ESR spectra of Ni-doped 3C-SiC

Electron Spin Resonance (ESR) spectra were recorded at different temperatures in the range of 110 K to 450 K to determine the actual spin state of Ni^{2+}ionand to get further insight on the microscopic origin of the magnetization in Ni-doped 3C-SiC. The ESR measurements were carried out using a JEOL X-band (frequency – 9.56 GHz) spectrometer with a rectangular cavity, 100 kHz field modulation, and phase-sensitive detection. The Ni^{2+} ion may occupy a substitutional Si^{4+} or Carbon site and may as well occupy interstitial sites. If a large fraction of Ni^{2+}

ions occupy substitutional Si sites then a sufficient number of Si vacancies have to be created for charge compensation. Besides, doping of Ni^{2+} is also expected to generate holes in the host matrix. The undoped 3C-SiC lattice itself shows the presence of defects as evidenced by the presence of a sharp ESR resonance corresponding to g = 2.00. The ground electronic state of Ni^{2+}, d^8 spin system is t_2 in a tetrahedral or distorted tetrahedral crystal field. Unless the distortion from T_d symmetry splits the doubly degenerate *e* levels far apart, the system is likely to be in a triplet ground state with $S = 1$. The ESR spectrum will correspond to a triplet ground state with g anisotropy and anisotropic zero-field splitting. The natural abundance of any magnetic Ni isotope ($I \neq 0$) being less than 1% no hyperfine splitting in the ESR spectrum is expected. Taking into consideration the orbital levels and occupancy it can be expected that, there are four electrons occupying the triple t_2 level with the net spin I = 1. The ESR spectra of all the Ni-doped samples show asymmetry and broadening of the peaks (Fig. 11 (a-c)). The asymmetry of the spectra shows the presence of structural distortion and the broadening of the peaks indicates ferromagnetic interactions in the system. The spectral line shape suggests that the 5% Ni-doped SiC has higher structural distortion compared to the 1% Ni-doped sample. The

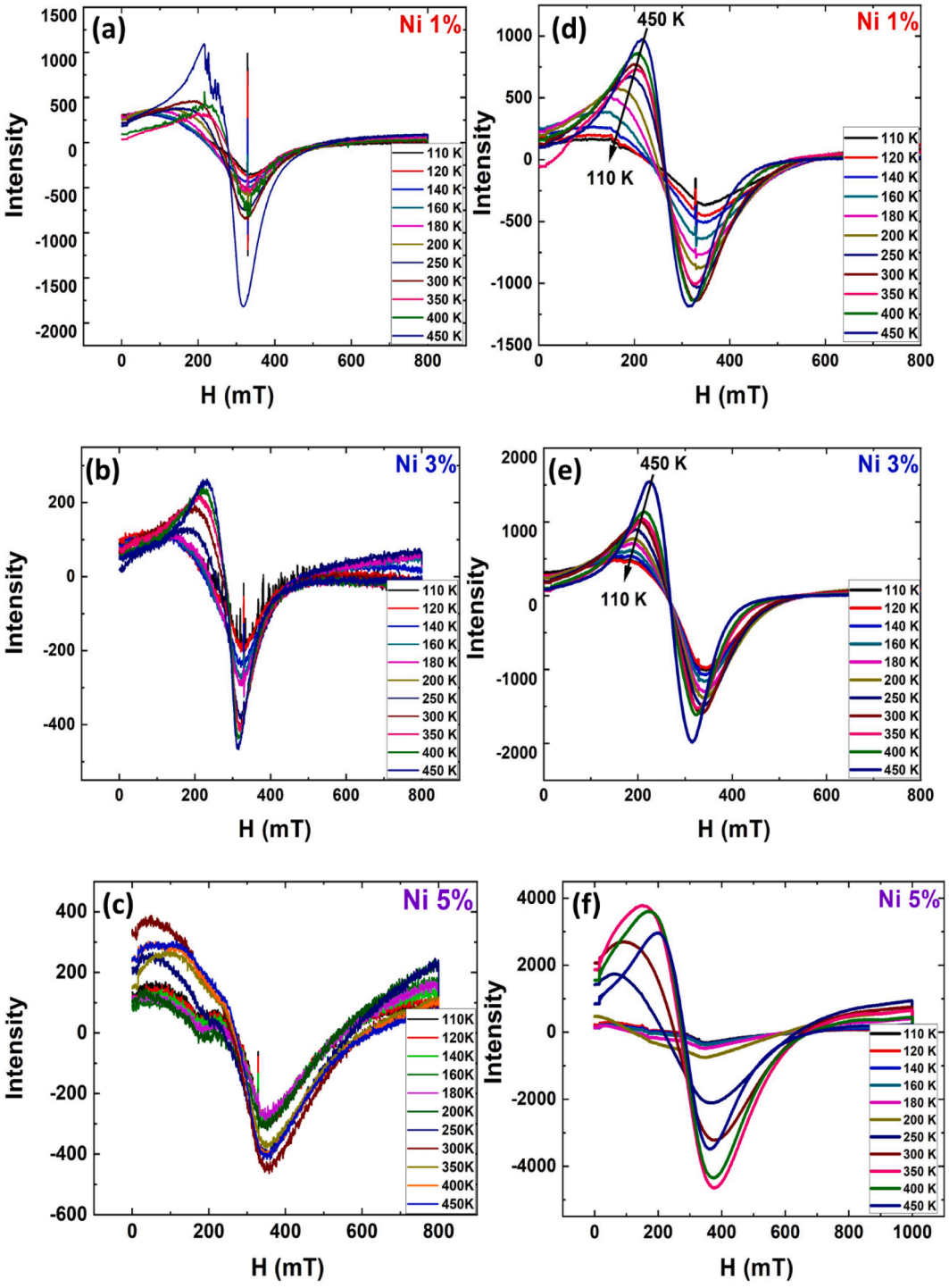

Fig. 11. (a - c) The ESR spectra of Ni-doped 3C-SiC samples recorded at different temperatures in the range of 110 K to 450 K on the as-prepared samples. (d, e, f) The spectra were recorded on samples annealed at 1200° C for 10 hrs.

anisotropy in the g factor is due to broken degeneracy. While the ESR spectra of 1% Ni^{2+} doped SiC shows broad asymmetric ESR lines with a sharp resonance at g = 2.00 arising out of defects, the spectra of 5% Ni^{2+} doped sample clearly shows broad asymmetric resonance with g less than 2.00 due to spin–orbit coupling mixing the levels within the t_2. The additional broad peak corresponding to g = 4.00 is presumed to be the 'forbidden transition' from Ms = − 1 to Ms = +1 of the spin-triplet which is the so-called 'double quantum transition' (Fig. 11 (a-c)).

The very broad anisotropic transition could be due to exchange broadening as well as an anisotropic zero-field splitting that will lead to an asymmetric ESR absorption in a randomly oriented D-tensor from a powder system. Additional broadening is caused by the anisotropic g-tensor. The ferromagnetic interactions aided by long-range exchange interactions between the Ni^{2+} impurity ions may be the reason for the absence of resolved g features in the spectra. The magnetic susceptibility measurements clearly support this claim. The spectra of all the annealed samples are more symmetric with reduced intensity of the sharp line due to electron-hole annihilation and diffusion of Ni^{2+} ions into low-energy substitutional sites. A detailed discussion on ESR spectra of annealed samples is given below.

6. Interpretation of ESR spectra of annealed samples

The ESR spectra of annealed samples (Fig. 11 (d, e, f)) show (i) reduction in line width (ii) increase in symmetric feature, and (iii) increase in intensity with rising temperature. But the ESR intensity of 5% Ni-doped sample shows a deviation from this behavior above a certain temperature. The spectral line width and its variation with temperature provide information about the magnetic interactions present in the system. Moreover, it also helps to understand the role played by magnetic dopants to set up magnetic order and gain insight into the relaxation dynamics present in the system. To extract more information about the system, the ESR spectra were fitted to Eq. (6).

$$S = L\frac{\Delta H^2}{(H_{ext} - H_r)^2 + \Delta H^2} + D\frac{\Delta H(H_{ext} - H_r)}{(H_{ext} - H_r)^2 + \Delta H^2} + C \quad (6)$$

Where, S → ESR Signal, L → Lorentzian Part, D → Dysonian Part, ΔH → Line width, H_r → Resonance Field, H_{ext} → External applied field, and C → Constant. The ESR spectra of annealed samples fitted to Eq. (6) are shown in Fig. 12 (a-c). The temperature variations of parameters obtained from the fit are shown in Fig. 13 (a, b).

The variation of ESR line width as a function of temperature for all the Ni-doped samples is shown in Fig. 13 (a). The broad spectrum in the low-temperature range could be attributed to the sum of the signals originating from Ni^{2+} ions and paramagnetic defects present in the host matrix.

The increase of line width with the decrease in temperature indicates that the number of interacting spins from Ni^{2+} ions increases when compared to the spins in paramagnetic centers. The structural defects that form during synthesis, dipolar interaction, and unresolved hyperfine interaction also play a very decisive role in the broadening of the ESR spectra as the temperature is lowered. The other possible

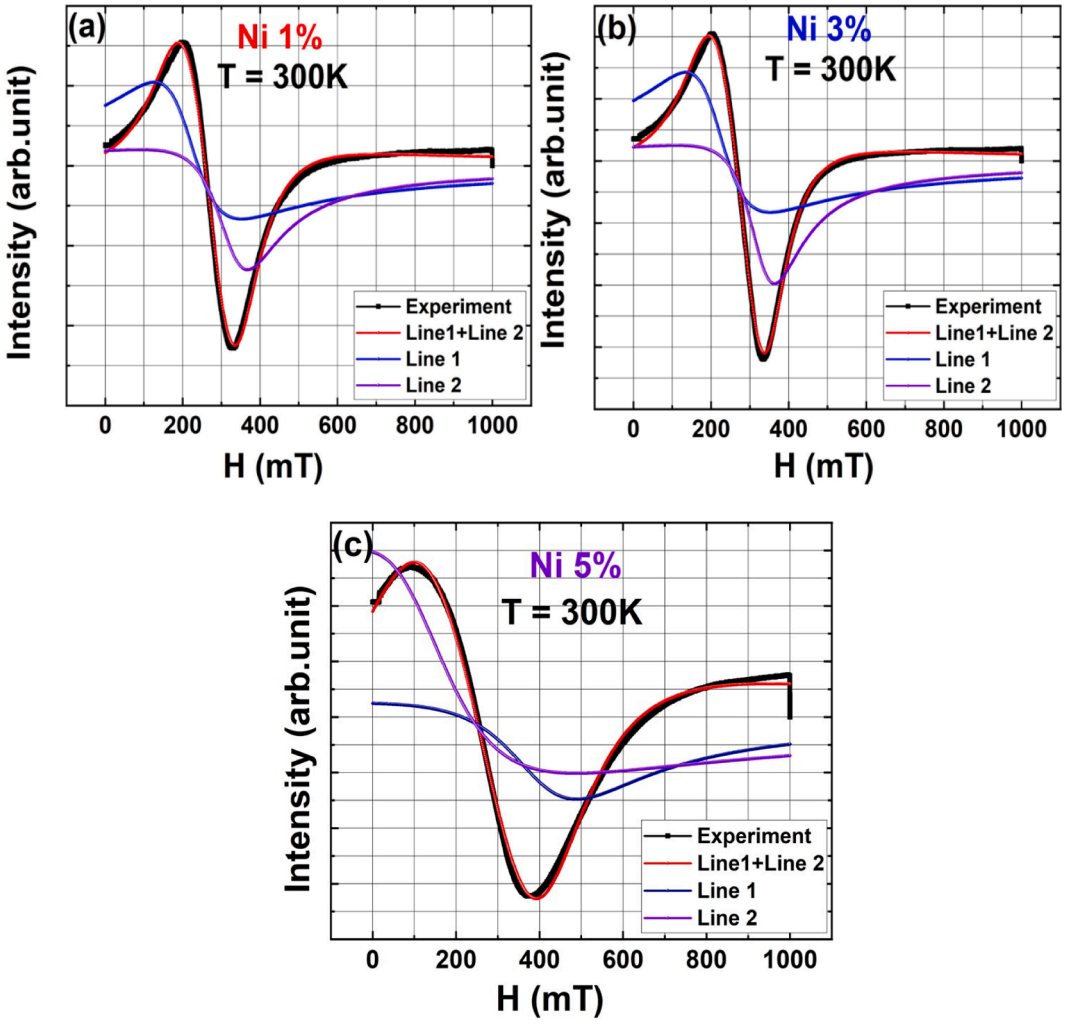

Fig. 12. ESR spectra of annealed Ni-doped 3C-SiC samples with fit to Eq. (6) and the Lorentzian and Dysonian Component obtained from the fit.

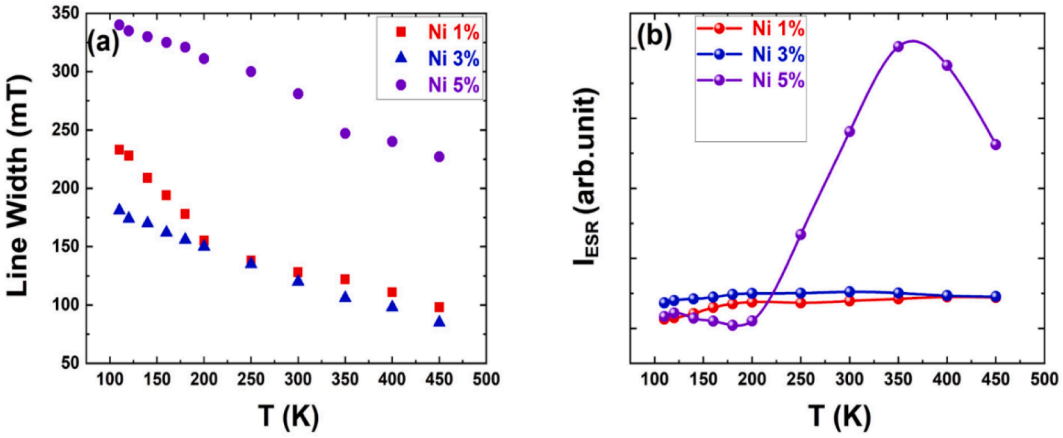

Fig. 13. **(a)** Variation of Line width and (b) Integrated Intensity of the ESR spectra of Ni-doped 3C-SiC samples with temperature.

contributions to spectral broadening are (i) the presence of charge compensating vacancies, (ii) local lattice strain due to fast spin–lattice relaxation time, and (iii) frozen spin profile which reflects as a disorder in the dipolar field and leads to the disproportionate increase in magnetization. The broadening of ESR line width has been reported in the family of the dilute magnetic semiconductors $Cd_{1-x}Mn_xSe_x$ and $Cd_{1-x}Mn_xTe_x$ [61,62]. The transition between spin sub-levels could contribute to the line broadening due to the small spin–spin relaxation time as compared to spin–lattice relaxation time. The temperature dependency of the integrated intensity of ESR spectra of all the Ni-doped samples is shown in Fig. 13 (b). The integrated intensity of 1% and 3% doped samples increases with rising temperature and does not follow usual Curie-like behavior at the higher temperature. But the Ni 5% doped sample follows Curie law above a particular temperature as shown in Fig. 13 (b). In this case, the integrated intensity of spectra increases with temperature from 110 K to 365 K, and after attaining a maximum at approximately 370 K, it decreases gradually with a further increase in temperature. An ideal paramagnetic ESR spectrum shows the reduction in intensity with the rise of temperature and follows Curie's law. But the presence of orbitally degenerate ground state and incomplete quenching of orbital angular momentum will result in deviation from the law [63]. As the temperature raises the spin–orbit coupling energy (K_BT) splits the orbitally degenerate ground state and lifts the degeneracy. This is the reason for the observed deviation in the variation of ESR intensity from Curie's law. The interaction energy of magnetic moments with the applied magnetic field became equal to the thermal energy (K_BT) of the atom at 365 K approximately [64]. This is the reason why there is a peak in the ESR intensity plot at 365 K in the 5% Ni-doped sample. With a further increase in temperature, thermal energy overcomes the interaction energy and randomizes the moments. This results in a reduction of paramagnetic susceptibility with the increase in temperature and the intensity plot follows usual Curie's law ($\chi = C/T$). Similar behavior in the temperature dependence of integrated intensity has been reported by Köseoğlu et al. [65]. All the Ni-doped samples show that the spins in the system are strongly coupled. The position of the peaks shifts towards lower fields with a decrease in temperature (Fig. 11 (d, e, f)) which could be due to strengthening of the magnetic interactions due to reduction in thermal fluctuations. The disappearance of the peak corresponding to g ~ 1.99 in the 5% Ni-doped can be attributed to the reduction of defect density due to annealing.

7. Conclusions

The Curie temperature of the doped samples has been found to be 420 K, 520 K, and 540 K respectively for Ni 1, 3, and 5% doping levels. The analysis of Raman spectra indicates the formation of defects, some local tetrahedral distortion as well as an increase in carrier concentration with the increase in Ni doping. The substitution of Ni^{2+} in place of Si^{4+} will result in the creation of vacancies. The intrinsic exchange interaction of Ni ions with Vsi, Vc, defects leads to ferromagnetic interactions. The room temperature ferromagnetism exhibited by Ni-doped 3C-SiC can be explained as a combined effect of orbital hybridization and magnetic impurity-mediated BMPs assuming a temperature-dependent BMP size.

CRediT authorship contribution statement

Gyanti Prakash Moharana: Investigation, Methodology, Writing. **Rahul Kothari:** Software. **S. K Singh:** Methodology. **P.D Babu:** Investigation. **Harish Kumar Narayanan:** Conceptualization, Supervision.

Declaration of Competing Interest

The authors declare that they have no known competing financial interests or personal relationships that could have appeared to influence the work reported in this paper.

Acknowledgment

One of the authors, Gyanti Prakash Moharana, thank IIT Madras for financial support. We greatly acknowledge IIT Madras and DST-SAIF for SQUID-VSM, and ESR measurements. We thank Professor: Sankaran Subramanian [Adjunct Professor & INSA Senior Scientist, Department of Chemistry & Sophisticated Analytical Instrument Facility] for useful discussion on the analysis of ESR spectra. Rahul Kothari is supported by the South African Radio Astronomy Observatory and the National Research Foundation (Grant No. 75415).

References

[1] B. Dieny, I.L.K. Prejbeanu, P. Garello, P. Gambardella, R. Freitas, W. Lehndorff, U. Raberg, S.O. Ebels, J. Demokritov, A. Akerman, P. Deac, C. Pirro, A. Adelmann, A.V. Anane, A. Chumak, S.M. Hirohata, S.O. Valenzuela, M. Cengiz Onbaşlı, M. d'Aquino, G. Prenat, G. Finocchio, L. Lopez-Diaz, R. Chantrell, O. Chubykalo-Fesenko, P. Bortolotti, Opportunities and challenges for spintronics in the microelectronics industry, Nat. Electron. 3 (2020) 446–459.
[2] A. Hirohata, K. Yamada, Y. Nakatani, I.-L. Prejbeanu, B. Dieny, P. Pirro, B. Hillebrands, Review on spintronics: Principles and device applications, J. Magn. Magn. Mater. 509 (2020), 166711.
[3] P. Barla, V.K. Joshi, S. Bhat, Spintronic devices: a promising alternative to CMOS devices, J. Comput. Electron. 20 (2021) 805–837.
[4] T. Dietl, H. Ohno, F. Matsukura, J. Cibert, D. Ferrand, Zener Model Description of Ferromagnetism in Zinc-Blende Magnetic Semiconductors, Science 287 (2000) 1019–1022.
[5] W. Prellier, A. Fouchet, B. Mercey, Oxide-diluted magnetic semiconductors: a review of the experimental status, J. Phys. Condens. Matter. 15 (2003) R1583–R1601.

[6] H. Ohno, Making Nonmagnetic Semiconductors Ferromagnetic, Science 281 (1998) 951–956.
[7] A.H. Macdonald, P. Schiffer, N. Samarth, Ferromagnetic semiconductors: moving beyond (Ga, Mn)As, Nat. Mater. 4 (2005) 195–202.
[8] M. Wang, R.P. Campion, A.W. Rushforth, K.W. Edmonds, C.T. Foxon, B. L. Gallagher, Achieving high Curie temperature in (Ga, Mn)As, Appl. Phys. Lett. 93 (2008), 132103.
[9] Sasanka. Deka, P.A. Joy, Synthesis and magnetic properties of Mn doped ZnO nanowires, Solid State Commun. 142 (2007) 190–194.
[10] M.L. Reed, N.A. El-Masry, H.H. Stadelmaier, M.K. Ritums, M.J. Reed, Room temperature ferromagnetic properties of (Ga, Mn)N, Appl. Phys. Lett. 79 (2001) 3473.
[11] A. Ben Mahmoud, H. J. von Bardeleben, J. L. Cantin, A. Mauger, E. Chikoidze, and Y. Dumont, Dumont, From ferromagnetic to antiferromagnetic interactions in n type $Zn_{1-x}Mn_xO$: An electron paramagnetic resonance study, Phys. Rev. B. 74 (2006) 115203.
[12] G. Prathiba, S. Venkatesh, N.H. Kumar, Structural, magnetic and semiconducting properties of Fe doped $SrSnO_3$, Solid State Commun. 150 (2010) 1436–1438.
[13] K. Balamurugan, N.H. Kumar, B. Ramachandran, M.S.R. Rao, J.A. Chelvane, P. N. Santhosh, Magnetic and optical properties of Mn-doped $BaSnO_3$, Solid State Commun. 149 (2009) 884–887.
[14] H. Saadaoui, X. Luo, Z. Salman, X.Y. Cui, N.N. Bao, P. Bao, R.K. Zheng, L.T. Tseng, Y.H. Du, T. Prokscha, A. Suter, T. Liu, Y.R. Wang, S. Li, J. Ding, S.P. Ringer, E. Morenzoni, J.B. Yi, Intrinsic Ferromagnetism in the Diluted Magnetic Semiconductor Co:TiO_2, Phys. Rev. Lett. 117 (2016) 227202–227206.
[15] L. Lin, R. Chen, C. He, H. Tao, J. Huang, L. Zhu, L. Yan, J. Zhang, Magnetic and optical properties of (Mn, Co) co-doped SnO_2, Vacuum 182 (2020), 109681.
[16] N. Mamouni, F. Goumrhar, E. Salmani, A. Benyoussef, H. Ez-Zahraouy, O. Mounkachi, Spin-orbit interaction in SnO_2 based diluted magnetic semiconductor: Ab-initio calculations, J. Magn. Magn. Mater. 535 (2021), 168084.
[17] L. Lin, R. Chen, J. Huang, P. Wang, H. Tao, Z. Zhang, Adsorption of gas molecules of CH_4, CO and H_2O on the vanadium dioxide monolayer: computational method and model, J. Phys. Condens. Matter 33 (2021), 055502.
[18] F.u. Ling, L. Yan, L. Lin, K. Xie, L. Zhu, C. He, Z. Zhang, Fe-embedded Au (111) monolayer as an electrocatalyst for N_2 reduction reaction: A first-principles investigation, J. Alloys. Comps. 875 (2021), 159907.
[19] L. Lin, Z. Shi, J. Huang, P. Wang, Y.u. Weiyang, C. He, Z. Zhang, Molecular adsorption properties of CH_4 with noble metals doped onto oxygen vacancy defect of anatase TiO_2 (101) surface: First-principles calculations, J. Apsusc. 514 (2020), 145900.
[20] Yu Li, Gang Wang, Shunchong Wang, Jianhui Yang, Liang Chen, Xiubo Qin, Bo Song, Baoyi Wang, and Xiaolong Chen, Defect-Induced Magnetism in Neutron Irradiated 6H-SiC Single Crystals. Phys. Rev. Lett. 106 (2011) 087205.
[21] Yutian Wang, Yu Liu, Gang Wang, Wolfgang Anwand, Catherine A. Jenkins, Elke Arenholz, Frans Munnik, Ovidiu D. Gordan, Georgeta Salvan, Dietrich R. T. Zahn, Xiaolong Chen, Sibylle Gemming, Manfred Helm and Shengqiang Zhou, Carbon p Electron Ferromagnetism in Silicon Carbide. Sci. Rep. **5** (2015) 8999.
[22] Y. Wang, C. Liu, Y. Zhang, Progress of d^0 magnetism in SiC, J. Semicond. 38 (2017), 033006.
[23] S. Zhou, X. Chen, Defect-induced magnetism in SiC, J. Phys. D: Appl. Phys. 52 (2019), 393001.
[24] Y.u. Liu, Y.e. Yuan, F. Liu, R. Böttger, W. Anwand, Y. Wang, A. Semisalova, A. N. Ponomaryov, L.u. Xia, A.T. N'Diaye, E. Arenholz, V. Heera, W. Skorupa, M. Helm, S. Zhou, Interaction between magnetic moments and itinerant carriers in d^0 ferromagnetic SiC, Phys. Rev. Lett. 102 (2009), 017201.
[25] T.H. Peng, Y.F. Lou, S.F. Jin, W.J. Wang, X.L. Chen, Powder Diffr. 24 (2009) 311.
[26] V.B. Shields, Application of silicon carbide for high temperature electronics and sensors, Jet Propuls Lab (1995) 1–9. https://trs.jpl.nasa.gov/handle/2014/31708.
[27] Randall Kirschman, High-Temperature Electronics, John Wiley & Sons/IEEE Press. (1998/1999) ISBN: 0-7803-3477-9.
[28] Raghavaratx Venkata Krishnarao, Yashwant Ramchandra Mahajan and Thimmani Jagadish Kumar, Conversion of Raw Rice Husks to SiC by Pyrolysis in Nitrogen Atmosphere, J. Eur. Ceram. Soc. 18 (1998) 147–152.
[29] N. Theodoropoulou, A.F. Hebard, S.N.G. Chu, M.E. Overberg, C.R. Abernathy, S. J. Pearton, R.G. Wilson, J.M. Zavada, Y.D. Park, Magnetic and structural properties of Fe, Ni, and Mn-implanted SiC, Journal of Vacuum Science & Technology A: Vacuum, Surfaces, and Films. 20 (2002) 579–582.
[30] B. Song, J.K. Jian, H. Li, M. Lei, H.Q. Bao, X.L. Chen, G. Wang, New experimental evidence for the origin of ferromagnetism ordering in Fe doped SiC, Physica B. 403 (2008) 2897–2901.
[31] S.B. Ma, Y.P. Sun, B.C. Zhao, P. Tong, X.B. Zhu, W.H. Song, Magnetic properties of Mn-doped cubic silicon carbide, Physica B. 394 (2007) 122–126.
[32] B.o. Song, H. Bao, H. Li, M. Lei, J. Jian, J. Han, X. Zhang, S. Meng, W. Wang, X. Chen, Magnetic properties of Mn-doped 6H-SiC, Appl. Phys. Lett. 94 (2009) 102508–102513.
[33] G.P. Moharana, S.K. Singh, P.D. Babu, Harish Kumar Narayanan, Investigation of magnetic order and spin dynamics in Mn-doped 3C-SiC, J. Alloys. Compd. 765 (2018) 314–323.
[34] Z. Huang, Q. Chen, Magnetic properties of Cr-doped 6H-SiC single crystals, J. Magn. Magn. Mater. 313 (2007) 111–114.
[35] G.P. Moharana, S.K. Singh, P.D. Babu, H.K. Narayanan, Role of spin, phonon and plasmon dynamics on ferromagnetism in Cr doped 3C-SiC, J. Magn. Magn. Mater. 491 (2019), 165505.
[36] F.u. Yuting, X. Jin, N. Sun, C. Li, Y. An, J. Liu, Effect of Ni doping and structural defects on magnetic properties of annealed SiC films, Superlattices and Microstructures. 96 (2016) 267–272.
[37] B. Song, X.L. Chen, J.C. Han, G. Wang, H.Q. Bao, L.B. Duan, K.X. Zhu, H. Li, Z. H. Zhang, W.Y. Wang, W.J. Wang, X.H. Zhang, S.H. Meng, Raman scattering and Magnetizations studies of (Al, Cr) – codoped 4H-SiC, J. Magn. Magn. Mater. 323 (2011) 2876–2882.
[38] S.K. Singh, B.C. Mohanty, S. Basu, Synthesis of SiC from rice husk in a plasma reactor, Bull. Mater. Sci. 25 (2002) 561–563.
[39] G. Mishra, S. Mohapatra, S. Prusty, M.K. Sharma, R. Chatterjee, S.K. Singh, D. K. Mishra, Magnetic properties of nanocrystalline beta-SiC, J. Nanosci. Nanotechnol. 11 (2011) 5049–5053.
[40] Biswajit Choudhury, RanjanaVerma, and Amarjyoti Choudhury, Oxygen defect assisted paramagnetic to ferromagnetic conversion in Fe doped TiO_2 nanoparticles, RSC Adv. **4** (2014) 29314-23.
[41] Brijmohan Prajapati, Shiv Kumar, Manish Kumar, S. Chatterjee, and Anup K. Ghosh, Investigation of the physical properties of Fe:TiO_2-diluted magnetic semiconductor nanoparticles, J. Mater. Chem. C. **5** (2017) 4257-67.
[42] M.B. Stearns, Y. Cheng, Determination of para and ferromagnetic components of magnetization and magnetoresistance of granular Co/Ag films (invited), J. Appl. Phys. 75 (10) (1994) 6894–6899.
[43] T. Ateeq Ahmed, M.N. Ali, A.A. Siddique, P. Tripathi, Enhanced room-temperature ferromagnetism in Ni-doped SnO_2 nanoparticles: A comprehensive study, J. Appl. Phys. 122 (8) (2017), 083906.
[44] Michael D. Kuz'min, Manuel Richter, Alexander N. Yaresko, Factors determining the shape of the temperature dependence of the spontaneous magnetization of a ferromagnet, Phys. Rev. B. **73** (2006) 100401.
[45] M. Bohra, P. Grammatikopoulos, R.E. Diaz, V. Singh, J. Zhao, J.-F. Bobo, A. Kuronen, F. Djurabekova, K. Nordlund, M. Sowwan, Surface segregation in chromium-doped NiCr alloy nanoparticles and its effect on their magnetic behavior, Chem. Mater. 27 (9) (2015) 3216–3225.
[46] J. Freeman, Dyson, Thermodynamic behavior of an ideal ferromagnet, Phys. Rev. 102 (1956) 1230–1244.
[47] J.M.D. Coey, M. Venkateshan, C.B. Fitzgerald, Donor impurity band exchange in dilute ferromagnetic oxide, Nat. Mater. 4 (2005) 173–179.
[48] C.P. Bean, J.D. Livingston, J. Appl. Phys. 30 (1959) 120S.
[49] W. Nathan, Gray and Ashutosh Tiwari, Dynamic superparamagnetism in cobalt doped Sm_2O_3 thin films, J. Appl. Phys. 110 (2011), 033903.
[50] W.F. Brown Jr., Theory of Approach to Magnetic Saturation, Phys. Rev. 58 (1940) 736–743.
[51] W.F. Brown Jr., The effect of dislocations on magnetization near saturation, Phys. Rev. 60 (1941) 139–147.
[52] L. Neel, Relation between the anisotropy constant and the saturation approach law for ferromagnetic, J. Phys. Radium. 9 (1948) 193–199.
[53] D.-L. Hou, X.-F. Nie, H.-L. Luo, Magnetic anisotropy and coercivity of ultrafine iron particles, J. Magn. Magn. Mater. 188 (1998) 169–172.
[54] A. Kaminski, S. Das Sarma, Polaron Percolation in Diluted Magnetic Semiconductors, Phys. Rev. Lett. 88 (2002) 247202–247204.
[55] B. Pal, P.K. Giri, High-temperature ferromagnetism and optical properties of Co-doped ZnO nanoparticles, J. Appl. Phys. 108 (2010) 084322–84328.
[56] H.S. Hsu, J.C.A. Huang, S.F. Chen, C.P. Liu, Role of grain boundary and grain defects on ferromagnetism in Co: ZnO films, Appl. Phys. Lett. 90 (2007) 102506–102513.
[57] R. Podila, W. Queen, A. Nath, J.T. Arantes, A.L. Schoenhalz, A. Fazzio, G. M. Dalpian, J. He, S.J. Hwu, M.J. Skove, A.M. Rao, Origin of FM Ordering in Pristine Micro- and Nanostructured ZnO, NanoLett. 10 (2010) 1383–1386.
[58] Z.L. Lu, H.S. Hsu, Y.H. Tzeng, F.M. Zhang, Y.W. Du, J.C.A. Huang, The origins of ferromagnetism in Co-doped ZnO single crystalline films: From bound magnetic polaron to free carrier-mediated exchange interaction, Appl. Phys. Lett. 95 (2009) 102501–102503.
[59] M. He, Y.F. Tian, D. Springer, I.A. Putra, G.Z. Xing, E.E.M. Chia, S.A. Cheong, T. Wua, Polaronic transport, and magnetism in Ag-doped ZnO, Appl. Phys. Lett. 99 (2011) 222511–222513.
[60] Y. Tian, Y. Li, M.i. He, Irwan Ade Putra, Haiyang Peng, Bin Yao, Siew Ann Cheong, and Tom Wu, Bound magnetic polarons and p-d exchange interaction in ferromagnetic insulating Cu-doped ZnO, Appl. Phys. Lett. 98 (2011) 162503–162513.
[61] S.B. Oseroff, Magnetic susceptibility and EPR measurements in concentrated spin-glasses: $Cd_{1-x}Mn_xTe$ and $Cd_{1-x}Mn_xSe$, Phys. Rev. B. 25 (1982) 6584–6594.
[62] A.M. Stoneham, K.A. MÃOEller, W. Berlinger. The temperature dependence of the line width of iron group ions in MgO. Solid State Commun, **10**(11): (1972) 1005 – 1008.
[63] Ibrahim BagudoMuh'd, Zainal A. Talib, Josephine Liew Ying Chyi. Mechanically induced defects in milled CdZnSe nanocrystal: A low-temperature electron spin resonance spectroscopy analysis. Results in Phys. **7** (2017) 1357 – 1360.
[64] J. Crangle. Solid State Magnetism. 1991.
[65] Y. Köseŏglu. Effect of surfactant coating on magnetic properties of Fe_3O_4 nanoparticles: ESR study. J. Magn. Magn. Mater (2006), 300 (1).